Boosting Seebeck coefficient through electron-phonon interaction by phonon frequency control

Asumi Michibata,[1] Tsukasa Terada,[1] Kotaro Matsuzono,[1] Takafumi Ishibe,[1] Yuichiro Yamashita,[2] Nobuyasu Naruse,[3] Katsuhiro Suzuki,[4] and Yoshiaki Nakamura[1,*]

[1]*Graduate School of Engineering Science, The University of Osaka, 1–3 Machikaneyama-cho, Toyonaka, Osaka 560–8531, Japan*
[2]*National Institute of Advanced Industrial Science and Technology, 1-1-1 Umezono, Tsukuba, Ibaraki 305–8563, Japan*
[3]*Department of Fundamental Bioscience (Physics), Shiga University of Medical Science, Otsu City, 520–2192, Japan*
[4]*Department of Mechanical Engineering, National Institute of Technology, Niihama College, 7-1 Yagumocho, Niihama, Ehime 792–0805, Japan*

(Received 27 November 2025; revised 29 January 2026; accepted 10 March 2026; published 3 April 2026)

In Dirac and Weyl semimetals with a flat band, the Seebeck coefficient (S) can be enhanced by the energy filtering effect in wave number space through electron-phonon interaction (EPI). Especially, topological B20-type semimetal thin films are promising materials because their Dirac or Weyl fermions are robust against defect scattering, making EPI dominant carrier scattering in the thin films. Here, we propose a strategy of raising this EPI-induced S enhancement effect (ESE) by enhancing EPI at room temperature (RT) via phonon frequency control. By using two atoms with a similar mass in topological B20 materials, the projected phonon density of states (DOS) of two atoms are mainly tuned within the frequency range below 200 cm^{-1} (RT thermal energy), leading to the increased total phonon DOS at RT related to EPI enhancement. In this study, focusing on topological B20-CoGe with Dirac-like and flat bands, where Co and Ge have similar masses, we demonstrate raising ESE in an epitaxial B20-CoGe thin film experimentally and theoretically. Although B20-CoGe is unstable under atmospheric pressure, the epitaxial growth of B20-CoGe thin films is achieved on Si substrates by the seed-assisted epitaxy method. The good agreement between experimental results and calculated S values with EPI is observed. The epitaxial B20-CoGe thin film shows the thermoelectric power factor of ~5.8 $\mu W\,cm^{-1}\,K^{-2}$, which is comparable to group IV element-based typical thermoelectric semiconductor thin films although B20-CoGe is a semimetal. Furthermore, the use of a heavier Ge atom resulted in lower thermal conductivity. The proposed strategy opens a new approach to realize a high thermoelectric performance (at RT) thin film on a Si platform.

DOI: 10.1103/lc66-t2m8

I. INTRODUCTION

Thermoelectric thin films on Si substrates, which can directly convert waste heat into electricity, are attracting considerable attention as stand-alone power sources for Internet-of-Things sensors on a Si platform [1–3]. Notably, it is highly anticipated to reuse the low temperature waste heat near room temperature (RT), which exists everywhere in large quantities. The thermoelectric conversion efficiency is evaluated by the dimensionless figure-of-merit: $zT = S^2\sigma T/\kappa$, where S is the Seebeck coefficient, σ is the electrical conductivity, κ is the thermal conductivity, and T is absolute temperature. Although both large $S^2\sigma$ and low κ are required to obtain high zT, it is challenging to simultaneously control these parameters (S, σ, κ) due to their intrinsic trade-off relationship [4–7]. Numerous studies have been reported to overcome this challenge through various strategies. Phonon scattering at interfaces is enhanced by introducing nanostructures, leading to drastically reduce κ [8–14]. On the other hand, the thermoelectric power factor ($S^2\sigma$) is increased through the quantum confinement effect, band convergence, resonant level effect, and energy filtering effects [15–22]. However, $S^2\sigma$ enhancement is limited due to carrier scattering by crystal defects such as impurities and interfaces, namely, degradation of the carrier mobility. For example, in the case of energy filtering in real space, electron scattering with low energy at interfaces occurs to enhance S [20–22].

Fermions in Dirac and Weyl semimetals of topological crystals are resistant to scattering by the defects, bringing high carrier mobility. Furthermore, in recent years, it has been reported that Dirac and Weyl semimetals show high $S^2\sigma$ due to their peculiar asymmetric electronic band structures: the Dirac-like bands and a flat band intersecting near the Dirac or Weyl points and Fermi level E_F [23–29]. Therein, high S arises from the energy filtering effect in the wave number (k) space in the following way. Conduction electrons with low energy in Dirac-like bands are preferentially scattered to the flat band with small carrier mobility due to strong electron-phonon interaction (EPI). As a result, energetic electrons mainly contribute to carrier transport, leading to the high S [Fig. 1(a)] [25,27–29]. Actually, Weyl semimetal B20-CoSi bulk, which has the peculiar asymmetric electronic structure at the Γ point, exhibits high $S^2\sigma$ through this EPI-induced S enhancement effect (ESE) [25,27,30].

Now, we notice that raising EPI strength is able to intensify the ESE in topological materials. Then, we are proposing a new strategy to raise EPI strength through phonon frequency

*Contact author: nakamura.yoshiaki.es@osaka-u.ac.jp

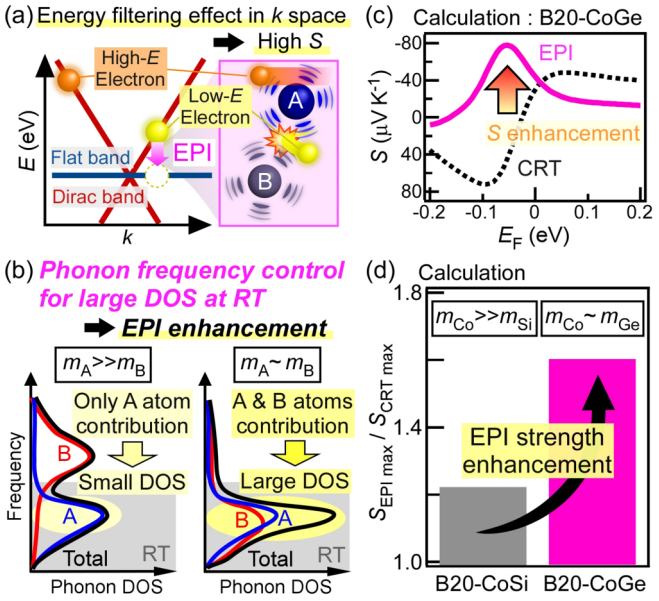

FIG. 1. (a) Schematic illustration of energy filtering in k space through EPI in topological materials with a peculiar electronic structure, leading to high S, namely ESE. (b) Schematic illustration of phonon frequency control for large phonon DOS at RT. In the case of $m_A \gg m_B$, only "A" atom contributes to the total DOS below the frequency of ~200 cm^{-1}, corresponding to RT. On the other hand, when $m_A \sim m_B$, both "A" and "B" atoms contribute to the total phonon DOS below the frequency of 200 cm^{-1}, leading to larger EPI strength. (c) Calculated S of B20-CoGe with EPI/CRT as a function of E_F through first-principles calculations. (d) Calculated enhancement ratios of S of B20-CoGe ($m_{Co} \sim m_{Ge}$) and B20-CoSi ($m_{Co} \gg m_{Si}$), which were calculated from the values in (c) and in Ref. [28], respectively.

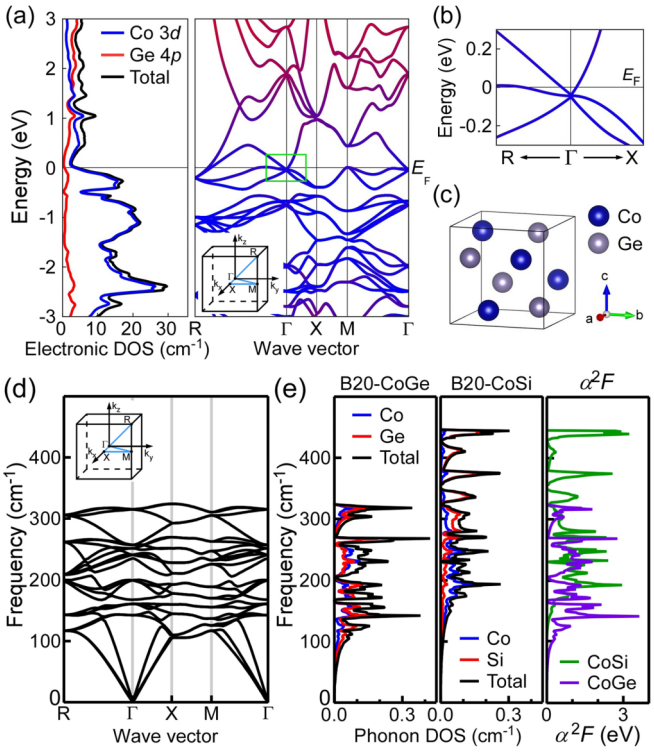

FIG. 2. (a) Calculated electronic band structure (right) and projected electronic DOS (the left) of B20-CoGe (red: Ge 4p and blue: Co 3d). (b) The enlarged graph of the square marked region (near E_F around the Γ point) in the right graph in (a). (c) Crystal structure of B20-CoGe. (d) Calculated phonon band structure. (e) Projected and total phonon DOSs of B20-CoGe (left) and B20-CoSi (middle). α^2F of B20-CoGe and B20-CoSi (right).

control; by selecting two atoms with similar masses in a topological B20-binary compound (B20 structure: the space group $P2_13$ [31]), phonon DOSs coming from two atoms' positions in the frequency range below 200 cm^{-1} (RT thermal energy) increasing the total phonon DOS in this frequency range. As a result, EPI strength, expressed as a phonon DOS-weighted quantity, is enhanced at RT due to the larger total phonon DOS [32] [Fig. 1(b)]. To confirm the validity of this strategy, we focus on B20-CoGe thin film ($m_{Co} \sim m_{Ge}$) as a topological material, instead of B20-CoSi thin film ($m_{Co} \gg m_{Si}$) [28]. Here, we make a preliminary check of ESE in B20-CoGe with a peculiar asymmetric electronic structure by comparing the S values we calculated with carrier relaxation time (τ) for EPI and with constant τ (CRT) [Fig. 1(c)], and we also confirmed that ESE is larger than that of B20-CoSi [28] [Fig. 1(d)] by comparing the S enhancement ratios of B20-CoGe and B20-CoSi, which were calculated from the values in Fig. 1(c) and in Ref. [28], respectively.

In this study, based on this strategy with the aforementioned preliminary theoretical evidence, we demonstrate large ESE in the epitaxial B20-CoGe thin film experimentally and theoretically. Therein, the seed-assisted epitaxy method [33] allows the epitaxial growth of B20-CoGe thin films on Si substrates although B20-CoGe is difficult to form under atmospheric pressure [34,35]. S is 1.6 times larger due to EPI than that with CRT. The $S^2\sigma$ of B20-CoGe thin film (~5.8 μW cm^{-1} K^{-2}) is comparable to group IV element-based typical thermoelectric semiconductor thin films such as $MnSi_\gamma$ [36] and β-$FeSi_2$ thin films [37] although B20-CoGe is a semimetal. Furthermore, instead of Si atoms, the use of heavier Ge atoms brought smaller κ. This indicates that the proposed strategy opens a new road to realize thermoelectric thin film generation for low temperature waste heat on a Si platform.

II. METHODS

Chemically cleaned undoped Si(111) substrates were introduced into a molecular beam epitaxy (MBE) chamber at a base pressure of approximately 3×10^{-8} Pa. Clean Si surfaces were prepared by epitaxial growth of Si buffer layers with 50 nm thickness on the undoped Si(111) substrates at 933 K after degassing at 773 K for 6 hours. Then, epitaxial B20-CoGe thin films were grown on clean Si(111) surfaces by seed-assisted epitaxy [33], which details are written below [Fig. 3(a)]. Five monolayers (MLs) of Ge were deposited on the cleaned Si(111) substrates at 673 K, and subsequently, 12 MLs of Co were deposited at 353 K. By annealing the Co/Ge layers at 473 K in the MBE chamber, nanoseeds of epitaxial B20-$CoSi_{1-x}Ge_x$ were formed, including diffused Si atoms from the Si substrates. Next, 50 nm thick B20-CoGe

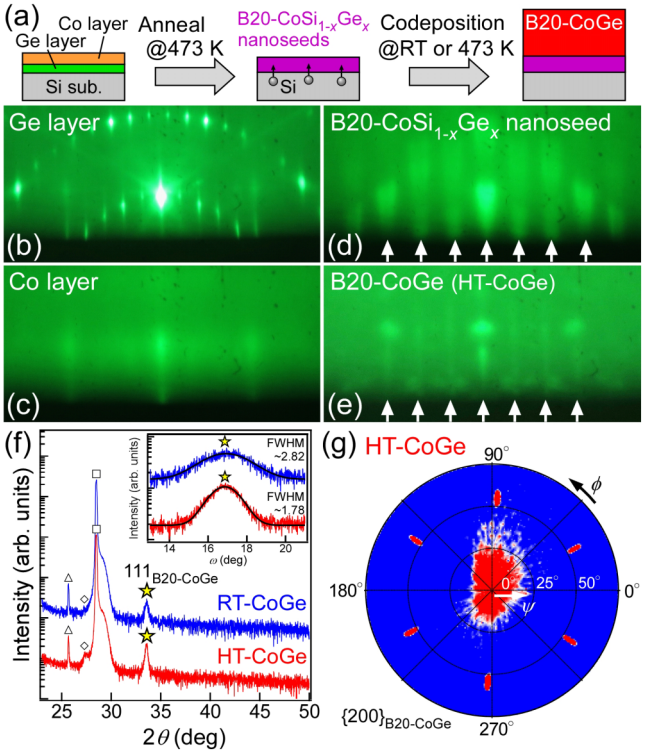

FIG. 3. (a) Seed-assisted epitaxy process of B20-CoGe film/Si. [(b)–(e)] RHEED patterns of Ge layer (5 MLs) (b), Co layer (12 MLs) (c), B20-$CoSi_{1-x}Ge_x$ nanoseeds (d), and B20-CoGe film (513 MLs) deposited at 473 K (e). The arrows in (d) and (e) denote the positions of diffraction spots coming from the B20 structure. (f) XRD 2θ-ω scans of HT-CoGe and RT-CoGe. The open stars denote the $111_{\text{B20-CoGe}}$ peaks. The open squares and the open triangles indicate the 111_{Si} peaks corresponding to the Cu K_α and K_β lines, respectively. The open diamond shapes indicate the 111_{Ge}. The inset in (f) is the XRD rocking curve of the $111_{\text{B20-CoGe}}$ peaks. (g) XRD pole figure of $\{200\}_{\text{B20-CoGe}}$ diffraction spots in HT-CoGe.

thin films were grown by codepositing Co (256.5 MLs) and Ge (256.5 MLs) on the B20-$CoSi_{1-x}Ge_x$ nanoseeds at RT or 473 K (referred as RT-CoGe or HT-CoGe, respectively). The epitaxy of B20-CoGe films on Si substrate was achieved only by using nanoseeds because B20-CoGe is only formed under high temperature and high pressure in general [34,35]. Some samples were post-annealed at 473, 523, or 573 K in an N_2 atmosphere, which are referred to as A-RT-CoGe or A-HT-CoGe.

Reflection high energy electron diffraction (RHEED) and high-resolution transmission electron microscopy (HRTEM) observations were carried out with 20 or 200 keV electron beams incident in the direction of $\langle 112\rangle_{\text{Si}}$, respectively. X-ray diffraction (XRD) measurement was conducted using Cu K_α line with the wavelength of 0.15418 nm. XRD pole figures were obtained under the condition that a tilt angle ψ varied from 0 to ~75° and a rotation angle ϕ varied from 0 to 360°. Hall carrier concentration n_{H}, σ, and S were measured in the in-plane direction using the Hall effect measurement method, van der Pauw method, and Seebeck coefficient measurement system (ADVANCE-RIKO Inc., ZEM-3), respectively. Based on the parallel conduction model, the contribution of the Si substrates to thermoelectric properties was considered, resulting in the negligible contribution of the Si substrates to measurements of S and σ due to the insulatorlike σ of the undoped substrates and high σ of semimetal B20-CoGe films (Sec. I in Ref. [38]). κ was measured in the out-of-plane direction using front-detection/front-heating type pulsed-light-heating time domain thermoreflectance (TDTR) method with a Mo transducer on the B20-CoGe film. The uncertainties of the S, σ, n_{H}, carrier mobility μ, $S^2\sigma$, and κ were estimated to be within ±7, ±1, ±10, ±10, ±15%, and ±30%, respectively, where the error of κ comes from an interfacial thermal resistance range of the Mo/B20-CoGe (1×10^{-10}–3×10^{-9} $m^2\,KW^{-1}$). First-principles calculations were performed on the PAW method using Quantum Espresso (Sec. II in Ref. [38]). The calculated result of B20-CoSi agreed with the previous one reported by one of the authors [27].

III. RESULTS

The calculated electronic band structure and projected electronic density of states (DOS) of B20-CoGe are shown in the right and left figures, respectively, in Fig. 2(a), and the crystal structure of B20-CoGe is shown in Fig. 2(c). The electronic band structure is similar to that of B20-CoSi and corresponds to that of B20-CoGe in previous reports [23,25,28,39–42]. It should be noted that the peculiar electronic structure is observed around the Γ point; Dirac-like and flat bands intersect near its crossing point of the Dirac-like linear band and E_{F}, as shown in Fig. 2(b), which is an enlarged graph of the square marked region in the right graph in Fig. 2(a). The calculated electronic DOS indicated that a pseudogap appears between 0.0 and 0.4 eV around E_{F} (gap ~ 0.4 eV). As shown in the left graph in Fig. 2(a), the main contribution of $3d$ states of Co atoms to bands near E_{F} indicates that a $3d$ electron of Co is dominant for the carrier transports in B20-CoGe.

Figures 2(d) and the left figure in Fig. 2(e) show the calculated phonon band structure and phonon DOS of B20-CoGe, respectively. Phonon modes in the frequency range below 200 cm^{-1}, which corresponds to RT thermal energy, originate from both Ge and Co atoms, which have similar atomic mass. On the other hand, in the case of B20-CoSi, the high-frequency range of phonons (>270 cm^{-1}) mainly comes from the vibrations of the lighter Si atoms, while the heavier Co atoms mainly contribute to the lower phonon frequency range below 200 cm^{-1} [the center figure in Fig. 2(e)]. As a result, in the RT thermal range, the phonon total DOS in B20-CoGe is larger than that in B20-CoSi. The right figure in Fig. 2(e) shows Eliashberg spectrum (α^2F) of B20-CoGe and B20-CoSi, related to EPI strength, respectively. In the RT thermal range (below 200 cm^{-1}), the α^2F value of B20-CoGe is significantly higher than that of B20-CoSi, suggesting larger EPI due to the larger phonon DOS coming from both contributions of Co and Ge.

To confirm the ESE of B20-CoGe experimentally, we fabricated B20-CoGe thin films by seed-assisted epitaxy [Fig. 3(a)]. Figure 3(b) shows the RHEED pattern after 5 MLs of Ge deposition. A (5 × 5) surface reconstruction pattern was observed, indicating that flat Ge film was

epitaxially grown on Si substrate. Figure 3(c) shows the RHEED pattern after 12 MLs of Co deposition, where the amount of Co deposition is larger than that of deposited Ge (Co/Ge deposition ratio = 2.4). To form the nanoseeds, the samples were annealed, where the RHEED pattern became clearer and spottier, as shown in Fig. 3(d). The RHEED patterns agreed with the theoretical ones of B20-$CoSi_{1-x}Ge_x$ showing the epitaxial relationship of $(111)_{\text{B20-CoSi}_{1-x}\text{Ge}_x}//(111)_{\text{Si}}$ with $[1\bar{1}0]_{\text{B20-CoSi}_{1-x}\text{Ge}_x}//[11\bar{2}]_{\text{Si}}$ or $[\bar{1}10]_{\text{B20-CoSi}_{1-x}\text{Ge}_x}//[11\bar{2}]_{\text{Si}}$, which analysis is elaborated in Sec. III of Ref. [38]. This indicated B20-$CoSi_{1-x}Ge_x$ nanoseeds were epitaxially grown due to the diffusion of Si atoms from Si substrates into B20-CoGe nanoseeds through annealing. It was also observed that the $\{11\bar{2}\}$ lattice plane spacing on RHEED streak spacing decreased with increasing annealing temperature, indicating that the amount of Si atoms diffusing from the Si substrate increased with increasing annealing temperature (Sec. III in Ref. [38]). Intriguingly, when a Co and Ge deposition ratio is a stoichiometric ratio (12 MLs of Co/12 MLs of Ge: Co/Ge = 1.0), the diffraction spots were not observed, indicating amorphous CoGe formation (Sec. IV in Ref. [38]). From these results, the growth of single-phase B20-CoGe nanoseeds is difficult due to the instability of B20-CoGe, while the growth of B20-CoSiGe on Si(111) is done by a Ge-poor deposition rate (Co/Ge ∼ 2.4). Formation of B20-structure *MX* (*M* = Cr, Mn, Fe, Co, …; *X* = Ge, …) is considered to be governed in the viewpoint of the atomic radius ratio of *M* to *X*, based on the previous research [34]. Therefore it is difficult to directly form stoichiometric B20-CoGe nanoseeds on a Si substrate, while alloying to the CoSiGe is effective for achieving epitaxial growth of the B20 crystal structure on the Si substrate.

After that, we conducted the seed-assisted epitaxy; Co and Ge with a stoichiometric ratio (Co/Ge = 1.0) were codeposited on the B20-$CoSi_{1-x}Ge_x$ nanoseeds at RT or 473 K to form B20-CoGe films (referred as RT-CoGe or HT-CoGe, respectively). Figure 3(e) shows the RHEED pattern after codeposition at 473 K. As is the case with the nanoseeds, the diffraction spots of the B20-structure were observed, indicating the formation of B20-CoGe thin films, where the lattice plane spacing was roughly consistent with the theoretical one of B20-CoGe (Sec. III in Ref. [38]). This reveals that there is no Si diffused from the substrate into the films. The RHEED patterns after codeposition at RT also showed similar but indistinct B20 structure diffraction spots (Sec. V in Ref. [34]). On the other hand, RHEED patterns of B20-CoGe were not observed without nanoseeds (Sec. VI in Ref. [38]). It should be noted that the B20-CoGe thin film was not epitaxially grown without the nanoseeds, indicating the necessity of nanoseeds for the epitaxial growth of B20-CoGe on the Si substrate.

XRD measurements were carried out for the RT-CoGe and HT-CoGe. XRD 2θ-ω scans displayed a $111_{\text{B20-CoGe}}$ peak at 2θ of ∼33.4° in addition to the peak coming from a Si substrate in each sample [Fig. 3(f)]. In HT-CoGe, a very small 111_{Ge} peak appears. The full width at half maximum (FWHM) of the rocking curve for the $111_{\text{B20-CoGe}}$ in HT-CoGe is smaller than that in RT-CoGe [the inset of Fig. 3(f)]. This indicates that a higher deposition temperature leads to a higher crystallinity accompanying with small Ge segregation. We

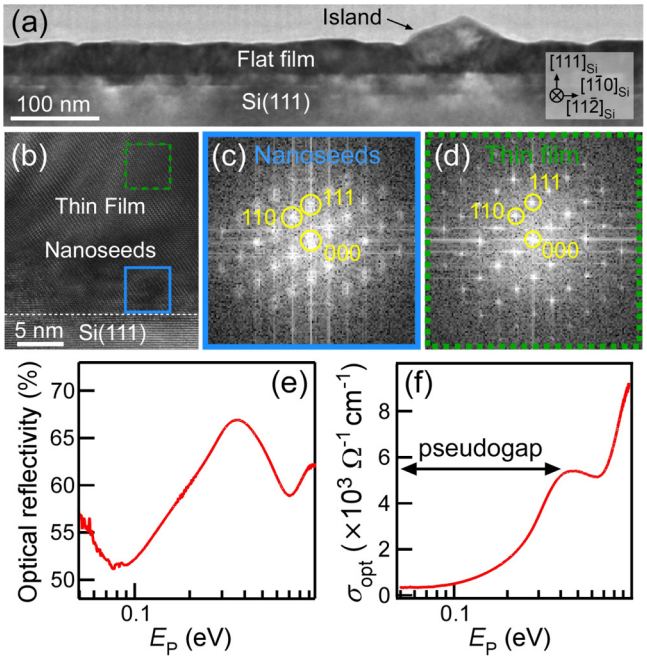

FIG. 4. (a) Cross-sectional HRTEM image of the epitaxial B20-CoGe film/Si (HT-CoGe). (b) Enlarged HRTEM image near the substrate interface. [(c) and (d)] FFT patterns of the solid (c) and dashed square regions (d) in (b), respectively. [(e) and (f)] Optical reflectivity (e) and σ_{opt} (f) of the epitaxial B20-CoGe film/Si (HT-CoGe).

carried out XRD pole figure measurements of these samples. Figure 3(g) shows the pole figure of HT-CoGe. The pole figure displayed sixfold symmetric peaks although the B20-CoGe crystal is threefold symmetrical to $[111]_{\text{B20-CoGe}}$ axis. This indicates the presence of a twin crystal rotated by 180° on a Si(111) substrate. This result was also obtained with RT-CoGe (Sec. V in Ref. [38]).

Figure 4(a) shows a cross-sectional HRTEM image of the HT-CoGe. An island and a flat film part are observed in the HT-CoGe with a thickness of ∼50 nm. Island parts are various Ge-rich regions such as $CoGe_2$ and Ge or stable monoclinic Ge-rich CoGe due to Ge segregation, resulting in the composition deviation of Ge-Co (Co rich composition) in the flat film parts (Secs. VII and VIII in Ref. [38]). Fig. 4(b) shows an enlarged HRTEM image near the interface between flat film region and Si substrate. It was found that there are two regions in a film part: thin film and nanoseeds. Fast Fourier transform (FFT) analyses were performed for the dashed and the solid square regions in Fig. 4(b), which results are displayed in Figs. 4(c) and 4(d), respectively. Both FFT patterns corresponded to the B20 structure with different details; The FFT pattern in the nanoseeds region [Fig. 4(c)] has lightly broader spot spacing than those in the thin film region [Fig. 4(d)]. The lattice space analysis revealed that the FFT patterns of the thin film (the nanoseeds) region corresponded to the theoretical ones of B20-CoGe (B20-$CoSi_{1-x}Ge_x$) with the epitaxial relationship of $(111)_{\text{B20-CoGe}}//(111)_{\text{Si}}((111)_{\text{B20-CoSi}_{1-x}\text{Ge}_x}//(111)_{\text{Si}})$ (Sec. IX in Ref. [38]). These results were consistent with the observation of RHEED and XRD results.

Next, to check if the formed B20-CoGe thin films have the electronic structure predicted by theoretical calculation, we experimentally measured the optical properties of the HT-CoGe. The optical conductivity σ_{opt} [Fig. 4(f)] was acquired from the optical reflectivity spectrum obtained using a Fourier transform infrared spectroscopy (FTIR) apparatus [Fig. 4(e)]. The σ_{opt} was very small below the optical energy E_P of ∼0.1–0.2 eV and rapidly increased with the increase of E_P. This rapid increase with the maximum value at E_P of ∼0.4 eV corresponds to the pseudogap (∼0.4 eV) of CoGe predicted by calculation. In addition, σ_{opt} further increased above E_P of ∼0.7 eV, which is consistent with the existence of a large DOS around E_P of ∼1.0 eV in the calculated electronic DOS with a peculiar electronic structure. These results suggest that epitaxial B20-CoGe thin films in this study have an electronic band structure similar to the theoretically predicted one.

We show thermoelectric properties of RT-CoGe, HT-CoGe, A-RT-CoGe, and A-HT-CoGe in Fig. 5. Here, we use n_H, that is, an effective carrier concentration as a variable of thermoelectric properties because n_H can be acquired both by experiments and calculation. In general, thermoelectric properties strongly depend on the carrier concentration. However, the carrier concentration definition of a semimetal is difficult, so there are some descriptions [28,43]. In the previous works with only electron packets near E_F, carrier concentration was approximately calculated from the electronic DOS by considering thermal energy, where the precise comparison with n_H was difficult because of the different definitions. In this study, the comparison between the experimental and calculation results was achieved by using calculated and experimental n_H with the same definition (Hall coefficient $R_H = 1/qn_H$ with the carrier charge q). This approach could serve as an important method for understanding the thermoelectric properties of semimetallic materials. The calculation detail is described in Sec. II of Ref. [38].

The calculated thermoelectric properties are directly dependent on the E_F [Fig. 1(c)]. The relationship between the E_F and the n_H is calculated as shown in the inset of Fig. 5(a) and Fig. S2 in Sec. II of Ref. [38]. Figure 5(a) shows S of B20-CoGe thin films as a function of n_H at RT. The calculated S - n_H curves using τ for EPI and a constant τ (CRT) were also plotted. In calculation, the two values of S at the same n_H are attributed to the same n_H value at different E_F. S values in B20-CoGe thin films agree well with the calculated ones [the upper curve denoted by the purple solid line in Fig. 5(a)] for EPI. To clarify this behavior, we discuss the relationship among E_F, n_H, and S in the EPI case. From EDX measurement (Fig. S8 in Ref. [38]), the flat film parts in HT-CoGe, where carrier transport mainly occurs, have a more Co rich composition (Co/Ge ∼ 1.3) than those in RT-CoGe (Co/Ge ∼ 1.1). Since Co atoms are considered to act as an electron donor, the E_F in HT-CoGe could be higher than that in RT-CoGe. In contrast, the experimentally measured n_H of HT-CoGe is lower than that of RT-CoGe. This decrease in n_H accompanying an upward shift of the E_F is consistent with the behavior of calculated n_H in the E_F range from −0.15 to −0.05 eV [the inset in Fig. 5(a)], which corresponds to the upper S-n_H curve (the purple solid line) in the EPI case in Fig. 5(a). Based on the above discussion, the relationships between S and n_H in B20-CoGe thin films agree well with the calculated ones for EPI, indicating that the carrier transport is dominated by EPI.

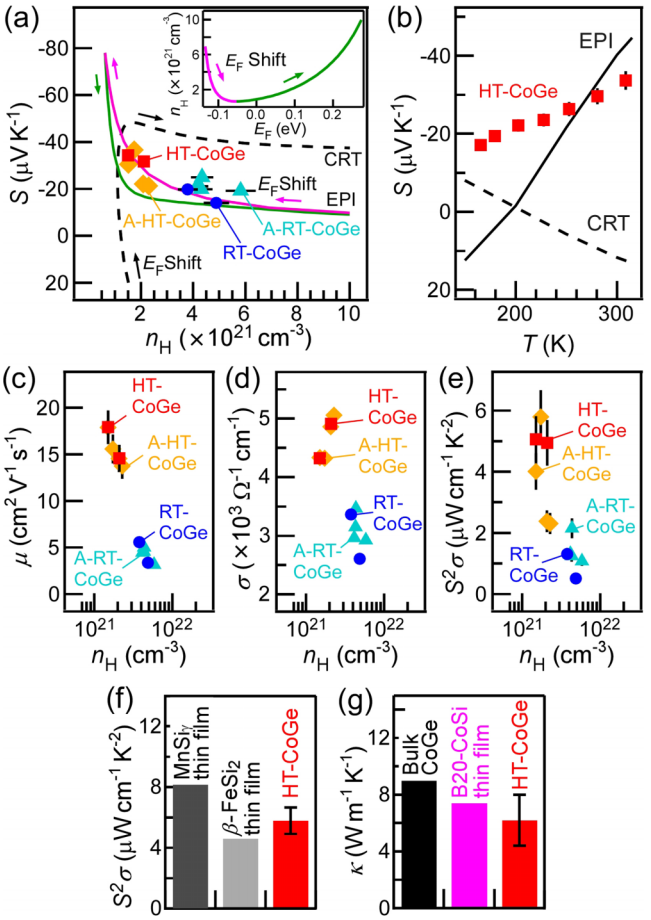

FIG. 5. (a) S of B20-CoGe thin films as a function of n_H. The solid and the dashed curves are the calculated S-n_H curve using τ for EPI and a constant τ, respectively. The relationship between the n_H and E_F (the inset). (b) S of HT-CoGe as a function of T. The calculated S curves using τ for EPI (the solid curve) and a constant τ (the dashed curve) are simultaneously plotted. [(c)–(e)] μ (c), σ (d), and $S^2\sigma$ (e) of B20-CoGe thin films as a function of n_H. (f) $S^2\sigma$ comparison between HT-CoGe and typical group IV element-based thermoelectric semiconductor thin films [36,37]. (g) κ of HT-CoGe with those of B20-CoGe bulk [23] and B20-CoSi film [28].

To confirm the carrier transport mechanism, we measured the temperature dependence of S of HT-CoGe with $n_H = 1.51 \times 10^{21}$ cm^{-3} in the range of 160–300 K [Fig. 5(b)]. We also plotted the calculation results using τ for EPI and constant τ, respectively. Therein, the E_F of the HT-CoGe was −0.01 eV at RT, which was determined from calculation and experimental data in Fig. 5(a). At higher temperature near RT, experimental S roughly agreed well with the calculated one for EPI, while at lower temperature, experimental S is deviating from the calculation for EPI to that for CRT. This deviation could come from the weaker EPI due to the phonon number decrease at low temperature. This result clearly indicates that EPI is dominant for the carrier transport in B20-CoGe thin films at RT. Incidentally, we confirmed that the effect of Ge precipitates on the S was negligible (Sec. XI in Ref. [38]).

Figures 5(c) and 5(d) show the μ and σ of B20-CoGe thin films as a function of n_H at RT. HT-CoGe exhibited higher σ than RT-CoGe due to higher μ. B20-CoGe thin films in this study show higher σ than conventional thermoelectric materials (1000–2000 $W^{-1}\,cm^{-1}$), such as Bi_2Te_3, PbTe, etc. [44–47]. Due to Ge precipitates, the performance presented here may be underestimated, and the single-phase B20-CoGe thin films could potentially exhibit superior properties (Sec. XI in Ref. [38]). We measured the post-annealing temperature dependence of n_H, S, μ, and σ, and no dependence was found (Sec. X in Ref. [38]). This indicates that the thermoelectric properties are independent of the crystallinity, supporting that the EPI is a main scattering mechanism in this topological material with strong resistance to defect scattering. Figure 5(e) shows $S^2\sigma$ of B20-CoGe thin films as a function of n_H at RT. The highest $S^2\sigma$ is ~5.8 $\mu W\,cm^{-1}\,K^{-2}$. Even higher $S^2\sigma$ is expected through optimization of n_H (at smaller n_H). The $S^2\sigma$ of B20-CoGe thin film is comparable to group IV element-based typical thermoelectric semiconductor thin films although B20-CoGe is a semimetal [Fig. 5(f)] [36,37].

Although the measurement direction is different from that of S and σ, the out-of-plane κ of the HT-CoGe was measured to be 6.2 $W\,m^{-1}\,K^{-1}$ by TDTR method. The anisotropy of the thermal conductivity in the present films with ~50 nm thickness is presumably negligible because of the cubic crystal structure of B20-CoGe and their thickness [48,49]. This value is lower than that of polycrystalline B20-CoGe bulk (~9.0 $W\,m^{-1}\,K^{-1}$) [23] and epitaxial B20-CoSi thin film (~7.4 $W\,m^{-1}\,K^{-1}$) [28] [Fig. 5(g)]. κ was divided into lattice thermal conductivity κ_L and electrical thermal conductivity κ_e using Wiedemann Franz law. Lorenz number L of B20-CoGe has not been reported, and it has been reported that L exceeds $L_0 = 2.44 \times 10^{-8}\,W\Omega\,K^{-2}$ in B20-CoSi with the peculiar asymmetric electronic structure [50]. Therefore, we used L_0 to evaluate κ_L as the maximum possible value. Also, since B20-CoGe has a cubic crystal structure, the in-plane and out-of-plane σ are considered to be equivalent. Therefore we used the in-plane σ in the Wiedemann–Franz law for estimating out-of-plane κ_L. It was found that κ_L of HT-CoGe was ~2.6 $W\,m^{-1}\,K^{-1}$, which is lower than those of polycrystalline B20-CoGe bulk (~5.7 $W\,m^{-1}\,K^{-1}$) [23] and epitaxial B20-CoSi thin film (~3.5 $W\,m^{-1}\,K^{-1}$) [28]. The reduction in κ_L in the B20-CoGe bulk may be due to phonon scattering on the film/substrate interface. The reduction in κ_L in the epitaxial B20-CoSi thin film is likely attributed to the fact that Ge is a heavier atom than Si, leading to a decrease in phonon group velocity. On the other hand, κ_e of HT-CoGe is relatively high (~3.6 $W\,m^{-1}\,K^{-1}$), which is higher than that of the epitaxial B20-CoSi thin film (~3.5 $W\,m^{-1}\,K^{-1}$) mainly due to the high n_H. This indicates that even lower κ could be achieved by reducing n_H to the same or lower than that of epitaxial B20-CoSi thin films.

IV. CONCLUSIONS

This study demonstrates the validity of the new strategy of phonon frequency control to enhance ESE experimentally and theoretically. The projected phonon DOS of B20-CoGe calculations revealed that both Ge atoms and Co atoms with similar atomic mass mainly contribute to the phonon mode in the frequency range below 200 cm^{-1} (RT thermal energy), leading to a large phonon DOS related to enhancing EPI. B20-CoGe thin films were epitaxially grown on Si substrates by seed-assisted epitaxy. The S as a function of n_H elucidated the agreement between experiments and calculations for EPI. As a result, the B20-CoGe thin films exhibited $S^2\sigma$ of ~5.8 $\mu W\,cm^{-1}\,K^{-2}$ at RT, which is comparable to group IV element-based typical thermoelectric semiconductor thin films although B20-CoGe is a semimetal.

In addition, the κ of HT-CoGe (6.2 $W\,m^{-1}\,K^{-1}$) was lower than that of polycrystalline B20-CoGe bulk (~9.0 $W\,m^{-1}\,K^{-1}$) and epitaxial B20-CoSi thin film (~7.4 $W\,m^{-1}\,K^{-1}$), which is attributed to the thin film structure and a heavier Ge atom than Si. The strategy phonon frequency control in topological materials opens a new road to realize thermoelectric thin film generation for low temperature waste heat on the Si platform.

ACKNOWLEDGMENTS

A part of this study was supported by a Grant-in-Aid for Scientific Research (No. 23H00258 and No. 21H04635), for Scientific Research B (No. 23K26056), and for Early-Carrier Scientists (No. 24K17613). This study was also partly supported by JST-CREST (No. JPMJCR1524).

DATA AVAILABILITY

The data that support this study's findings are available within the article.

[1] N. Jaziri, A. Boughamoura, J. Müller, B. Mezghani, F. Tounsi, and M. Ismail, A comprehensive review of thermoelectric generators: Technologies and common applications, Energy Reports **6**, 264 (2020).

[2] Md. N. Hasan, M. Nafea, N. Nayan, and M. S. Mohamed Ali, Thermoelectric generator: Materials and applications in wearable health monitoring sensors and internet of things devices, Adv. Mater. Technol. **7**, 2101203 (2022).

[3] H. Xie, Y. Zhang, and P. Gao, Thermoelectric-powered sensors for internet of things, Micromachines **14**, 31 (2023).

[4] L. D. Hicks and M. S. Dresselhaus, Thermoelectric figure of merit of a one-dimensional conductor, Phys. Rev. B **47**, 16631 (1993).

[5] G. J. Snyder, M. Christensen, E. Nishibori, T. Caillat, and B. B. Iversen, Disordered zinc in Zn_4Sb_3 with phonon-glass and electron-crystal thermoelectric properties, Nat. Mater. **3**, 458 (2004).

[6] A. J. Minnich, M. S. Dresselhaus, Z. F. Ren, and G. Chen, Bulk nanostructured thermoelectric materials: Current research and future prospects, Energy Environ. Sci. **2**, 466 (2009).

[7] T. Mori, Novel principles and nanostructuring methods for enhanced thermoelectrics, Small **13**, 1702013 (2017).

[8] X. Tang, W. Xie, H. Li, W. Zhao, Q. Zhang, and M. Niino, Preparation and thermoelectric transport properties of high-performance p-type Bi_2Te_3 with layered nanostructure, Appl. Phys. Lett. **90**, 012102 (2007).

[9] J.-K. Yu, S. Mitrovic, D. Tham, J. Varghese, and J. R. Heath, Reduction of thermal conductivity in phononic nanomesh structures, Nat. Nanotechnol. **5**, 718 (2010).

[10] K. Biswas, J. He, Q. Zhang, G. Wang, C. Uher, V. P. Dravid, and M. G. Kanatzidis, Strained endotaxial nanostructures with high thermoelectric figure of merit, Nat. Chem. **3**, 160 (2011).

[11] Y. Nakamura, M. Isogawa, T. Ueda, S. Yamasaka, H. Matsui, J. Kikkawa, S. Ikeuchi, T. Oyake, T. Hori, J. Shiomi, and A. Sakai, Anomalous reduction of thermal conductivity in coherent nanocrystal architecture for silicon thermoelectric material, Nano Energy **12**, 845 (2015).

[12] Y. Nakamura, Nanostructure design for drastic reduction of thermal conductivity while preserving high electrical conductivity, Sci. Technol. Adv. Mater. **19**, 31 (2018).

[13] X. Huang, S. Gluchko, R. Anufriev, S. Volz, and M. Nomura, Thermal conductivity reduction in a silicon thin film with nanocones, ACS Appl. Mater. Interfaces **11**, 34394 (2019).

[14] T. Taniguchi, T. Terada, Y. Komatsubara, T. Ishibe, K. Konoike, A. Sanada, N. Naruse, Y. Mera, and Y. Nakamura, Phonon transport in the nano-system of Si and SiGe films with Ge nanodots and approach to ultralow thermal conductivity, Nanoscale **13**, 4971 (2021).

[15] Y. Uematsu, T. Ishibe, T. Mano, A. Ohtake, H. T. Miyazaki, T. Kasaya, and Y. Nakamura, Anomalous enhancement of thermoelectric power factor in multiple two-dimensional electron gas system, Nat. Commun. **15**, 322 (2024).

[16] S. Xie, W. Liu, X. Wan, J. Lyu, F. Yan, Y. Ouyang, X. Li, Y. Liu, Z. Wang, R. Wang, J. Wu, Q. Zhang, and X. Tang, Rational manipulation of epitaxial strains enabled valence band convergence and high thermoelectric performances in Mg_3Sb_2 films, Adv. Funct. Mater. **33**, 2300154 (2023).

[17] G. Tan, F. Shi, S. Hao, H. Chi, L.-D. Zhao, C. Uher, C. Wolverton, V. P. Dravid, and M. G. Kanatzidis, Codoping in SnTe: Enhancement of thermoelectric performance through synergy of resonance levels and band convergence, J. Am. Chem. Soc. **137**, 5100 (2015).

[18] A. Shibagaki, R. Hotta, T. Ishibe, Y. Yamashita, N. Naruse, Y. Mera, and Y. Nakamura, Controlling thermoelectric properties of epitaxial GeSn film/Si by tuning strain and composition, Appl. Phys. Lett. **126**, 231601 (2025).

[19] S. Sakane, T. Ishibe, K. Mizuta, T. Fujita, Y. Kiyofuji, J. Ohe, E. Kobayashi, and Y. Nakamura, Anomalous enhancement of thermoelectric power factor by thermal management with resonant level effect, J. Mater. Chem. A **9**, 4851 (2021).

[20] S. Sakane, T. Ishibe, T. Taniguchi, N. Naruse, Y. Mera, T. Fujita, M. M. Alam, K. Sawano, N. Mori, and Y. Nakamura, Thermoelectric power factor enhancement based on carrier transport physics in ultimately phonon-controlled Si nanostructures, Mater. Today Energy **13**, 56 (2019).

[21] D. Vashaee and A. Shakouri, Improved thermoelectric power factor in metal-based superlattices, Phys. Rev. Lett. **92**, 106103 (2004).

[22] J. H. Bahk, Z. Bian, and A. Shakouri, Electron energy filtering by a nonplanar potential to enhance the thermoelectric power factor in bulk materials, Phys. Rev. B **87**, 075204 (2013).

[23] N. Kanazawa, Y. Onose, Y. Shiomi, S. Ishiwata, and Y. Tokura, Band-filling dependence of thermoelectric properties in B20-type CoGe, Appl. Phys. Lett. **100**, 093902 (2012).

[24] D. A. Pshenay-Severin, Y. V. Ivanov, and A. T. Burkov, The effect of energy-dependent electron scattering on thermoelectric transport in novel topological semimetal CoSi, J. Phys.: Condens. Matter **30**, 475501 (2018).

[25] Y. Xia, J. Park, F. Zhou, and V. Ozoliņš, High thermoelectric power factor in intermetallic CoSi arising from energy filtering of electrons by phonon scattering, Phys. Rev. Appl. **11**, 024017 (2019).

[26] Y. Xia, J. Park, V. Ozoliņš, and C. Wolverton, Leveraging electron-phonon interaction to enhance the thermoelectric power factor in graphene-like semimetals, Phys. Rev. B **100**, 201401 (2019).

[27] H. N. Nam, K. Suzuki, A. Masago, H. Shinya, T. Fukushima, and K. Sato, The role of electron–phonon scattering on thermoelectric properties of intermetallic compounds XSi (X = Co, Rh), Jpn. J. Appl. Phys. **62**, 020904 (2023).

[28] T. Ishibe, T. Hinakawa, S. Sakane, S. Ishigaki, K. Suzuki, K. Sato, T. Fujita, Y. Yamashita, E. Kobayashi, and Y. Nakamura, Robust thermoelectric power factor enhanced by energy filtering effect in B20-type CoSi films, Phys. Rev. Mater. **9**, 075402 (2025).

[29] Z. Li, K. Pal, H. Lee, C. Wolverton, and Y. Xia, Electron–phonon interaction mediated gigantic enhancement of thermoelectric power factor induced by topological phase transition, Nano Lett. **24**, 5816 (2024).

[30] H. Sun, X. Lu, and D. T. Morelli, Effects of Ni, Pd, and Pt substitutions on thermoelectric properties of CoSi alloys, J. Electron. Mater. **42**, 1352 (2013).

[31] S. Basak, A. Kobiałka, M. Sternik, J. Łażewski, P. T. Jochym, A. M. Oleś, P. Piekarz, and A. Ptok, Electronic and dynamical properties of cobalt monogermanide CoGe phases under pressure, Comput. Mater. Sci. **244**, 113149 (2024).

[32] J. P. Carbotte, Properties of boson-exchange superconductors, Rev. Mod. Phys. **62**, 1027 (1990).

[33] T. Terada, R. Kitaura, S. Ishigaki, T. Ishibe, N. Naruse, Y. Mera, R. Asahi, and Y. Nakamura, Seed-assisted epitaxy of intermetallic compounds with interface-determined orientation: Incommensurate Nowotny chimney-ladder $FeGe_\gamma$ epitaxial film, Acta Mater. **236**, 118130 (2022).

[34] H. Takizawa, T. Sato, T. Endo, and M. Shimada, High-pressure synthesis and electrical and magnetic properties of MnGe and CoGe with the cubic B20 structure, J. Solid State Chem. **73**, 40 (1988).

[35] V. I. Larchev and S. V. Popova, The polymorphism of transition metal monogermanides at high pressures and temperatures, J. Less-Common Met. **87**, 53 (1982).

[36] Q. R. Hou, Z. M. Wang, and Y. J. He, Thermoelectric properties of manganese silicide films, Appl. Phys. A **80**, 1807 (2005).

[37] T. Taniguchi, S. Sakane, S. Aoki, R. Okuhata, T. Ishibe, K. Watanabe, T. Suzuki, T. Fujita, K. Sawano, and Y. Nakamura, Thermoelectric properties of epitaxial β-$FeSi_2$ thin films on Si(111) and approach for their enhancement, J. Electron. Mater. **46**, 3235 (2017).

[38] See Supplemental Material at http://link.aps.org/supplemental/10.1103/lc66-t2m8 for negligible contribution of Si substrates to thermoelectric properties, calculation methods, annealing effect on the lattice plane spacing of B20-$CoSi_{1-x}Ge_x$ nanoseeds and the lattice plane spacing of B20-CoGe thin film, nanoseeds formed by deposition of Co and Ge in a stoichiometric ratio, B20-CoGe grown on B20-$CoSi_{1-x}Ge_x$ nanoseeds at room temperature, need of the nanoseeds for growth of B20-CoGe thin film on Si, analysis of the island parts in HT-CoGe, composition in the flat film parts and the island parts, lattice plane spacing difference between the regions of the nanoseeds and the flat thin film in HT-CoGe, effect of the post-annealing on thermoelectric properties, the influence of the island parts on thermoelectric properties, and Wannier functions of 3*d* electron of Co, which includes Refs. [23,51–63].

[39] A. Sakai, F. Ishii, Y. Onose, Y. Tomioka, S. Yotsuhashi, H. Adachi, N. Nagaosa, and Y. Tokura, Thermoelectric power in transition-metal monosilicides, J. Phys. Soc. Jpn. **76**, 093601 (2007).

[40] M. A. Timaoui, H. Bouafia, B. Sahli, S. Hiadsi, B. Abidri, A. Bouaza, A. Akriche, and D. Kerroum, FP-(L)APW + lo study of mechanical stability and electronic behavior of CoGe in B20 structure, Mater. Sci.-Pol. **35**, 548 (2017).

[41] C. K. Barman, C. Mondal, S. Pujari, B. Pathak, and A. Alam, Symmetry protection and giant Fermi arcs from multifold fermions in binary, ternary, and quaternary compounds, Phys. Rev. B **102**, 155147 (2020).

[42] G. I. Ameereh, B. A. Hamad, and J. M. Khalifeh, Electronic structure of Co (Si, Ge) compounds: *Ab-initio* calculation, Physica B **403**, 3503 (2008).

[43] T. Terada, Y. Uematsu, T. Ishibe, N. Naruse, K. Sato, T. Q. Nguyen, E. Kobayashi, H. Nakano, and Y. Nakamura, Giant enhancement of seebeck coefficient by deformation of silicene buckled structure in calcium-intercalated layered silicene film, Adv. Mater. Interfaces **9**, 2101752 (2022).

[44] W.-S. Liu, Q. Zhang, Y. Lan, S. Chen, X. Yan, Q. Zhang, H. Wang, D. Wang, G. Chen, and Z. Ren, Thermoelectric property studies on Cu-Doped *n*-type $Cu_xBi_2Te_{2.7}Se_{0.3}$ nanocomposites, Adv. Energy Mater. **1**, 577 (2011).

[45] X. Liu, T. Zhu, H. Wang, L. Hu, H. Xie, G. Jiang, G. J. Snyder, and X. Zhao, Low electron scattering potentials in high performance $Mg_2Si_{0.45}Sn_{0.55}$ based thermoelectric solid solutions with band convergence, Adv. Energy Mater. **3**, 1238 (2013).

[46] H. J. Wu, L.-D. Zhao, F. S. Zheng, D. Wu, Y. L. Pei, X. Tong, M. G. Kanatzidis, and J. Q. He, Broad temperature plateau for thermoelectric figure of merit ZT>2 in phase-separated $PbTe_{0.7}S_{0.3}$, Nat. Commun. **5**, 4515 (2014).

[47] X.-Y. Wang, H.-J. Wang, B. Xiang, L.-W. Fu, H. Zhu, D. Chai, B. Zhu, Y. Yu, N. Gao, Z.-Y. Huang, and F.-Q. Zu, Thermoelectric performance of Sb_2Te_3-based alloys is improved by introducing PN junctions, ACS Appl. Mater. Interfaces **10**, 23277 (2018).

[48] E. A. Scott, J. T. Gaskins, S. W. King, and P. E. Hopkins, Thermal conductivity and thermal boundary resistance of atomic layer deposited high-*k* dielectric aluminum oxide, hafnium oxide, and titanium oxide thin films on silicon, APL Mater. **6**, 058302 (2018).

[49] T. Ishibe, R. Okuhata, T. Kaneko, M. Yoshiya, S. Nakashima, A. Ishida, and Y. Nakamura, Heat transport through propagon-phonon interaction in epitaxial amorphous-crystalline multilayers, Commun. Phys. **4**, 153 (2021).

[50] L. Zhong, X. Jin, M. He, R. Wang, X. Zhou, T. Deng, and X. Yang, Phonon-dominated thermal transport and large violation of the Wiedemann-Franz law in topological semimetal CoSi, arXiv:2511.06290.

[51] P. Giannozzi, *et al.*, QUANTUM ESPRESSO: A modular and open-source software project for quantum simulations of materials, J. Phys.: Condens. Matter **21**, 395502 (2009).

[52] P. E. Blöchl, Projector augmented-wave method, Phys. Rev. B **50**, 17953 (1994).

[53] G. K. H. Madsen and D. J. Singh, BoltzTraP. A code for calculating band-structure dependent quantities, Comput. Phys. Commun. **175**, 67 (2006).

[54] G. Samsonidze and B. Kozinsky, Accelerated screening of thermoelectric materials by first-principles computations of electron–phonon scattering, Adv. Energy Mater. **8**, 1800246 (2018).

[55] S. Kirkpatrick, Percolation and conduction, Rev. Mod. Phys. **45**, 574 (1973).

[56] D. J. Bergman and L. G. Fel, Enhancement of thermoelectric power factor in composite thermoelectrics, J. Appl. Phys. **85**, 8205 (1999).

[57] S. Sakane, T. Ishibe, K. Mizuta, M. Kashino, K. Watanabe, T. Fujita, Y. Kamakura, N. Mori, and Y. Nakamura, Methodology of thermoelectric power factor enhancement by nanoscale thermal management in bulk SiGe composites, ACS Appl. Energy Mater. **3**, 1235 (2020).

[58] W. W. Tyler, R. Newman, and H. H. Woodbury, Properties of germanium doped with cobalt, Phys. Rev. **97**, 669 (1955).

[59] T. Taniguchi, T. Ishibe, H. Miyamoto, Y. Yamashita, and Y. Nakamura, Thermoelectric properties of epitaxial Ge thin films on Si(001) with strong crystallinity dependence, Appl. Phys. Express **11**, 111301 (2018).

[60] S. M. Sze and J. C. Irvin, Resistivity, mobility and impurity levels in GaAs, Ge, and Si at 300 °K, Solid State Electron. **11**, 599 (1968).

[61] C. J. Glassbrenner and G. A. Slack, Thermal conductivity of silicon and germanium from 3 °K to the melting point, Phys. Rev. **134**, A1058 (1964).

[62] N. Marzari and D. Vanderbilt, Maximally localized generalized Wannier functions for composite energy bands, Phys. Rev. B **56**, 12847 (1997).

[63] I. Souza, N. Marzari, and D. Vanderbilt, Maximally localized Wannier functions for entangled energy bands, Phys. Rev. B **65**, 035109 (2001).